Article

Solvent Effects on the Structural and Optical Properties of MAPbI₃ Perovskite Thin Film for Photovoltaic Active Layer

Saif M. H. Qaid *, Hamid M. Ghaithan, Bandar Ali Al-Asbahi and Abdullah S. Aldwayyan

Physics and Astronomy Department, College of Science, King Saud University, Riyadh 11451, Saudi Arabia; hghaithan@ksu.edu.sa (H.M.G.); balasbahi@ksu.edu.sa (B.A.A.-A.); dwayyan@ksu.edu.sa (A.S.A.)
* Correspondence: sqaid@ksu.edu.sa

Abstract: Controlling the crystallinity, homogeneity, and surface morphology is an efficient method of enhancing the perovskite layer. These improvements contribute toward the optimization of perovskite film morphology for its use in high-performance photovoltaic applications. Here, different solvents will be used in order to process the perovskite precursor, to improve the interfacial contacts through generating a smooth film and uniform crystal domains with large grains. The effect that the solvent has on the optical and structural properties of spin-coated methyl ammonium lead iodide (MAPbI₃) perovskite thin films prepared using a single-step method was systematically investigated. The spin-coating parameters and precursor concentrations of MAI and PbI₂ were optimized to produce uniform thin films using the different solvents N, N-dimethylformamide (DMF), dimethyl sulfoxide (DMSO), and γ-butyrolactone (GBL). The effect that the solvent has on the morphology of the MAPbI₃ films was examined to determine how the materials can be structurally altered to make them highly efficient for use in perovskite hybrid photovoltaic applications. Scanning electron microscopy (SEM) and X-ray diffractometry (XRD) results show that the synthesized MAPbI₃ films prepared using DMSO, DMF, and GBL exhibit the best crystallinity and optical characteristics (photoluminescence (PL)), respectively, of the prepared films. The optical properties resulting from the noticeable improvement PL of the films can be clearly correlated with their crystallinity, depending on the solvents used in their preparation. The film prepared in DMSO shows the highest transmittance and the highest bandgap energy of the prepared films.

Keywords: perovskite; CH₃NH₃PbI₃; solvent additive; morphology; optical properties; photovoltaics materials

1. Introduction

Organic-inorganic halide perovskites (OIHPs) have received much attention recently as potential light-absorbing materials for use in photovoltaic applications [1,2]. These materials have a wide absorption window from the visible to near-infrared region of the electromagnetic spectrum with the advantages of a strong absorption onset, high absorption and extinction coefficients, as well as band gaps that can be easily adjusted by changes to their composition [1,3–5]. OIHPs can transport both electrons and holes, with long charge carrier diffusion lengths that can exceed one micrometer [4]. The exciton binding energies of MAPbI₃ perovskite have been reported to vary from 37 to 50 meV [6–8], which is comparable to the thermal energy at ambient temperature (RT).

Many studies have found that controlling the crystallinity, homogeneity, and surface morphology of perovskites is an effective way of improving the perovskite layer to prepare materials that achieve high power conversion efficiencies in perovskite photovoltaics [1,2]. A high-quality perovskite layer can greatly reduce non-radiative recombination, which decreases both the open-circuit voltage (V_oc) and carrier lifetime [9]. The reason for the reduction in non-radiative recombination is that the perovskite layer has slow ionic transport properties and good charge transport, which prevent hysteresis behavior in current-voltage

(I–V) measurements, meaning that the free carriers can be effectively collected at the electrode [10]. Huge variations in the morphology of perovskites can be observed when they are allowed to precipitate in an uncontrolled way [11,12].

Several processing techniques have been proposed as effective methods for controlling the quality of perovskite layers, including solvent treatment methods, annealing methods [13] using temperature and humidity to form crystals, controlling the proportion of perovskite solution, moisture-assisted growth, additives, and hot spin-coating [14–16]. Moreover, the dependence of the morphological and optical properties on the deposition method used to prepare perovskite films has been studied. Many different deposition methods have been explored, such as the one/ two-step solution and vapor deposition methods [17–21].

All or some of these conditions and methods can be combined, as the annealing parameters greatly depend on the perovskite composition, as well as on the solvent [22–24]. So, annealing gives the perovskite molecules sufficient thermal energy to self-organize and form a well-ordered crystalline layer. If the annealing temperature is too low and the time is too short, then the prepared film may have relatively weak optical absorption and photoluminescence (PL) as the percentage of amorphous molecules is too great in this type of sample. However, the perovskite will be destroyed or decomposed if the annealing temperature is too high and the annealing time is too long.

The solvents DMF, DMSO, GBL, and N-methyl-2-pyrrolidone (NMP) have been shown to be effective solvents for preparing PbI_2 and CH_3NH_3I. In addition, mixed solvent systems have been investigated to optimize the perovskite layer morphology toward highly efficient perovskite hybrid photovoltaics [25]. A mixture solvent of DMSO/DMF was used in the perovskite precursor dissolution to achieve organic lead iodide (PbI_2) as an intermediate phase, which provides a unique treatment solution during film formation. As a result, the delay time during solvent treatment can be used to control the morphology and grain size of the perovskite film [26,27]. Other studies [28,29] have preferred mixed solvents over binary solvents (e.g., DMF/ DMSO or GBL/DMSO) due to the high solubility of the solvent/precursor ratio, which is the opposite of a single solvent. The single solvent prevents the formation of a dense film and leads to the low stability of perovskite solar cells (PSCs). Another group [30] established a binary solvent engineering technique (SET) for the formation of perovskite films that do not require thermal annealing, providing a new method for film preparation at RT and paving the way for the development of cheap and stable PSCs. DMF was used as a low boiling solvent in this method, and NMP (complexing agent) was utilized as a high boiling solvent with a higher Lewis basicity than DMF, making it more likely to react with PbI_2 and generate an intermediate phase. Liu et al. [31] developed and improved the PCE of PSCs using binary solvents by SET to fabricate a high-quality film (dense and uniform) by adding a small quantity of pyridine to DMSO/DMF as a mixed solution of $Cs_{0.05}(MA_{0.17}FA_{0.83})_{0.95}Pb(I_{0.83}Br_{0.17})_3$ perovskite precursor. Therefore, the introduction of pyridine to passivate the crystal's surface defects results in good coverage with pinhole-free, large grains, a low-resistance perovskite film, and a long charge carrier lifetime.

Comparing binary to ternary solvents, ternary mixed solvents are more commonly used to create a high-quality film (dense, pinhole-free, and big grain size). A 4:1 molar ratio of (NMP: DMSO/DMF) provides a method to manufacture more efficient PSCs [26,32].

Seok et al. used solvent engineering to prepare a pinhole-free film for use in inverted structure perovskite solar cells [33]. Jeon et al. reported the solution processing of efficient PSCs comprising a bilayered architecture and $MAPb(I_{1-x}Br_x)_3$ perovskites formed using SET [34]. In another reports [13], the optical (UV–vis and PL) and structural (IR) properties were found to be highly dependent on the perovskite layer prepared with different solvents. Another group has presented a set of solubility data for $MAPbBr_3$, $FAPbBr_3$ $MAPbI_3$, and $FAPbI_3$, perovskites in DMF and DMSO, and they rationalize the observed differences in solubility by analyzing the donor numbers of the solvents and halide anions [35].

In light of these reports, which detail a variety of approaches to improve the perovskite thin films by using SET, numerous groups interested in the development of high-quality perovskite films utilizing various SET have been able to accelerate their research. However, the pore-filling, poor coverage, and a large morphological diversity in perovskite, which is formed through uncontrolled precipitation, further hamper the development and future application of these materials in photovoltaic fields. So, the morphology and high-quality perovskite films are critical for the production of stable and efficient PSCs. Therefore, many technologies have been used to enhance the perovskite film morphology, such as spin coating, vacuum/ vapor deposition, and solvent engineering. Although vacuum deposition gives greater film homogeneity, solution-processing procedures (which are mostly carried out via spin coating) have distinct advantages, such as reduced costs and fewer scaling issues [1]. The SET method is one of the most effective methods for preparing films with high quality for stable and efficient PSCs. Moreover, the choice of solvent is critical for obtaining a dense, large grain size, uniform, and high-quality perovskite film due to its considerable effect on the morphology and properties of the film.

Here, the effect of aprotic solvent engineering (to dissolve the perovskite precursor and the fabricated MAPbI$_3$ films), due to their morphology, coverage ratio, PL efficiencies, and PL spectrum, will be investigated to understand and compare the ability of carriers to inject electrons into the perovskite layer with different films prepared by different solvents. From the PL spectrum analyses, it can be expected the electronic characteristics of the perovskite film such as the mobility and the majority carrier type [36]. This study will be demonstrated through a simple method for improving the reproducibility and controlling the morphological structure by increasing the perovskite coverage and reducing the formation of the pinholes. Moreover, the effect of Pb-rich/ poor conditions in PL efficiencies, PL spectra, and photo-stability will be examined and a general strategy for the optimization of perovskite films indicated.

In this study, high-quality perovskite films were prepared utilizing a one-step solution process with spin coating as the deposition technique, with the morphologies of the films adjusted using the different solvents GBL, DMF, and DMSO at low temperatures. Using ultraviolet (UV)-visible (vis)-near-infrared (NIR) absorption spectroscopy, PL spectroscopy, X-ray diffractometry (XRD), and scanning electron microscopy. The effect of the solvent on the structural quality and optical properties of the produced films was carefully examined (SEM). The produced films were also subjected to amplified spontaneous emission (ASE) tests.

2. Materials and Methods

2.1. Materials

The perovskite precursors methyl ammonium iodide (CH$_3$NH$_3$I, MAI) and lead iodide (PbI2), as well as the an-hydrous solvents N,N-dimethylformamide (DMF), dimethyl sulfoxide (DMSO), and γ-butyrolactone (GBL) used in the experiments, were acquired from Sigma Aldrich and used without further purification. The properties of the solvents are summarized in Table 1.

Table 1. Properties of the solvents studied in this work.

Name	Abbreviation	Formula	Density (g·mL^{-1})	Dipole Moment (Polarity) (Debye)
Dimethylformamide	DMF	C$_3$H$_7$NO	0.948	3.86
Dimethyl sulfoxide	DMSO	C$_2$H$_6$OS	1.1004	3.96
γ-Butyrolactone	GBL	C$_4$H$_6$O$_2$	1.1296	4.27

2.2. Methods

In this work, methyl ammonium lead iodide (CH$_3$NH$_3$PbI$_3$, MAPbI$_3$) perovskite was prepared as a precursor solution as previously reported in the literature [3,11,17–21,37], and

the solvent solution deposition of films of the perovskite was carried out via a spin-coating one-step deposition method. Until now, perovskite films have been deposited either under vacuum or through solution processing [17–21,38]. Despite the fact that vacuum deposition creates more uniform films, solution processing techniques have advantages, such as lower costs and fewer scaling issues. In this regard, the single-step solution approach used in this work is promising for controlling the synthesis of MAPbI₃.

Equimolar ratios of MAI and PbI₂ were mixed together in solvent to produce a 30 wt.% precursor solution of MAPbI₃, which was then stirred in an oven at 70 °C for 6 h.

For thin film deposition, glass substrates were first cleaned sequentially in an ultrasonic bath in detergent, de-ionized water, and ethanol for 15 min. After that, the solution was then spin-coated directly on the substrate (microscopic glass) to form a deposit. The film was then heat-treated to increase the degree of crystallinity of the sample and adjust its grain size. The sample was crystallized via annealing by heating the sample on a hotplate at 100 °C for 1 h in air. The excess MAI is assumed to be lost via evaporation during this process. After its thermal treatment, the resulting perovskite film was allowed to cool to room temperature, whereafter it was noticed that the color of the perovskite had changed from bright yellow to dark brown, suggesting that a perovskite crystal had formed. After the film was dried, the formed MAPbI₃ perovskite was analyzed using different techniques. A schematic chart of the perovskite layer deposition process is shown in Figure 1. Finally, perovskite films were directly deposited on microscopic glass as a substrate for all measurements.
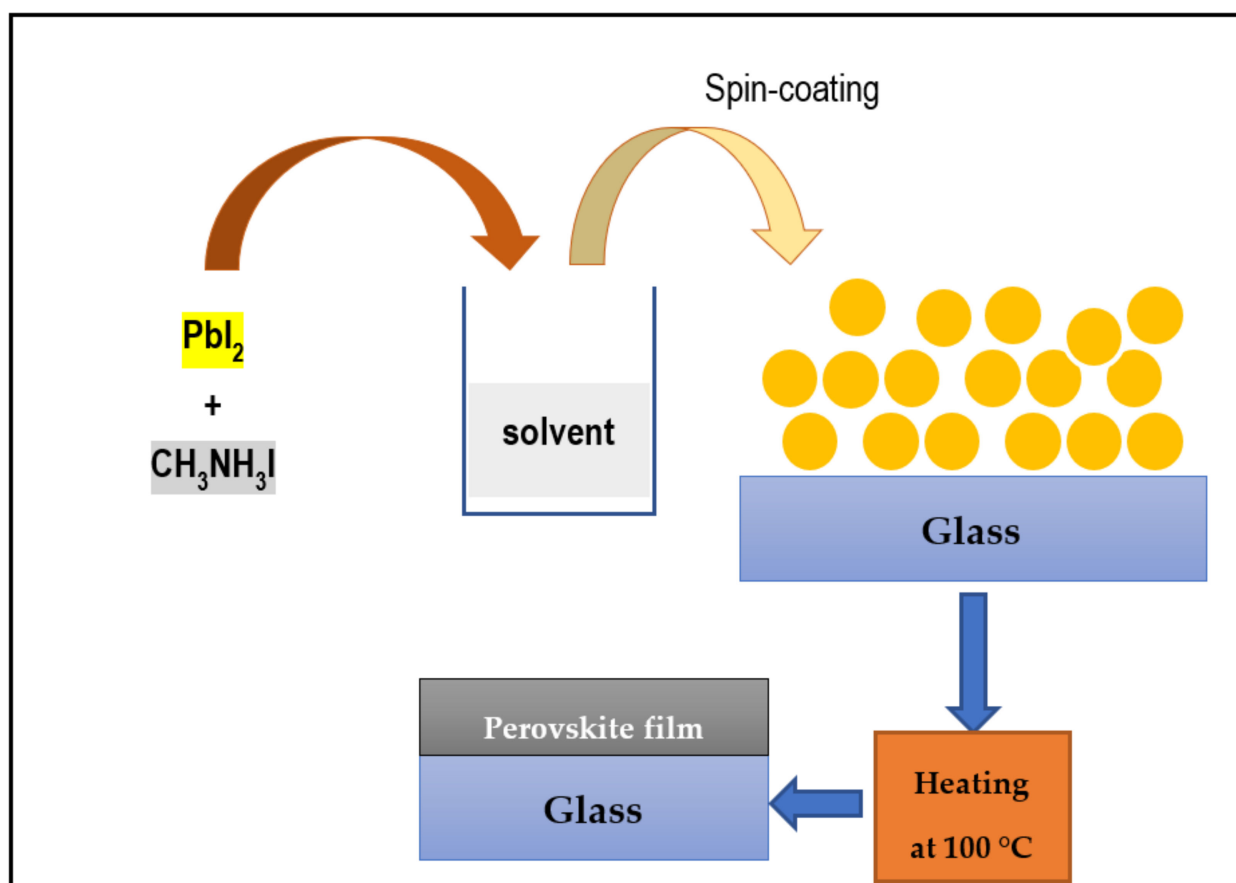
Figure 1. Schematic diagram of the deposition process used to prepare the perovskite film in this work.

2.3. Characterization

To examine the effects that the solvent has on the optical and structural properties of the synthesized samples, they were analyzed using different techniques. XRD and SEM were used to determine the crystallinity of the samples and to provide information on the particle size and surface morphology, respectively. The XRD patterns were collected us-ing an X-pert Pro MPD instrument (PANalytical Ltd., Cambridge, UK) diffractometer equipped with a CuKα radiation source (λ = 0.154 nm) operated at 15 mA and 40 kV over a 2θ range of 10–60° and the SEM images were collected using a JEOL-JSM-6380 SEM model microscope (JEOL, Tokyo, Japan). UV-vis-NIR spectra of the perovskite films were recorded using a Perkin Elmer (LAMBDA-40, Perkin-Elmer, Beaconsfield, UK) spectrometer in the range of 400–800 nm. The thin film thickness was measured by a surface profilometer (Dektak 150, Bruker Corp, Tucson, AZ, USA).

PL spectra of the perovskite films were recorded at an excitation wavelength of 532 nm and ASE was generated in the perovskite film using a Q-switched Nd: YAG nanosecond laser (Solara, LPS 1500, SolarLS JSC, Minsk, Belarus, 3rd harmonic, wavelength: 355 nm, pulse width: 11 ns, repetition rate: 100 Hz). Second harmonic generation (λ_{ex} = 532 nm) with a pulse width of 11 ns under varying pumping energies of 6–12 mJ were the exact parameters employed for this test. The ASE beam appeared as a cone of light at the ideal pump power and sample concentration. ASE spectra were collected using a 1 mm entrance slit of an intensified charge-coupled device camera (MS257 ICCD) detector (Lot Oriel Instruments, Stratford, CT, USA).

3. Results

3.1. Structural Characteristics

To investigate the effect that the solvent has on the performance of the film, the interconnected crystalline structure of the precursors, and the film morphology, 30 wt.% so-lutions of MAI and PbI_2 were spin-coated on glass substrates using GBL, DMF, and DMSO as the processing solvents. Figure 2 shows the XRD patterns of the $MAPbI_3$ perovskite films coated on glass substrates.
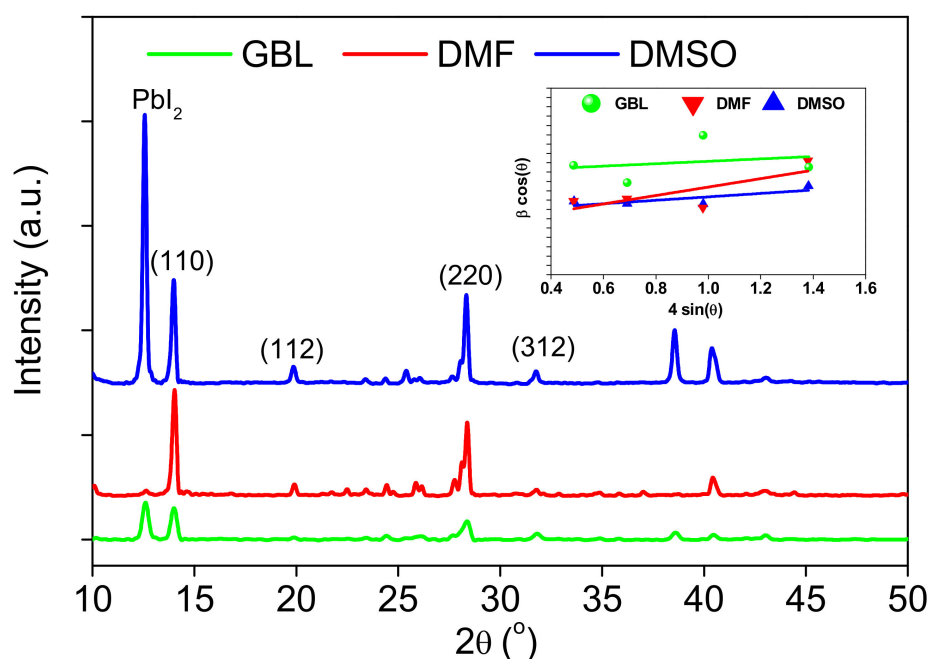
Figure 2. X-ray Diffraction patterns of the $MAPbI_3$ perovskite thin films were prepared using different solvents. The insets show a Uniform deformation mode plot which concluded from XRD spectra.

It can be seen that all films adopt a typical tetragonal (p4mm) and (I4cm) phase structure [39], with diffraction peaks at 14.01°, 19.87°, 28.38°, 31.80°, and 40.43°. The diffraction peaks can be assigned to the (110), (112), (220), (312), and (224) planes, respectively, with no differences in the positions of the peaks for all of the films, in agreement with the results published in previous reports [39,40]. The XRD spectrum of the film is shown PbI_2 at low angles ($2\theta \approx 12.8°$) in Figure 2. The appearance of the PbI_2 peak at low angles in XRD data was attributed to the deposition method [41]. Three alternative procedures have been used to produce a perovskite film using solution methods, including one-step deposition of mixed precursors, sequential solution deposition, and spray coating. Calcification using a one-step solution approach is a simple process with long-term photoluminescent features. The one-step approach to perovskite production is occasionally insufficient to convert PbI_2 to $MAPbI_3$. Meanwhile, the two-step coating approach was found to be sufficient for converting PbI_2 to $MAPbI_3$, as evidenced by the lack of a PbI_2 peak in the XRD spectrum [3,11]. The reason for this is that $MAPbI_3$ films were synthesized at room temperature by converting PbI_2 in a saturated solution of MAI in 2-propanol. Furthermore, the type of a typical polar solvent for PbI_2 is another effect to play a role in the appearance of PbI_2 peaks in XRD data [10]. The PbI_2 peak was stronger for DMSO rather than GBL and DMF (DMF is a common polar solvent for perfectly dissolved PbI_2).

Then, a modified model of the Williamson–Hall (W-H) analysis, namely the uniform deformation model (UDM) plot which was concluded from XRD spectra, was used to extract the values of both strain and particle size. The instrumental broadening (profile correction) in the XRD was measured through the following relation:

$$\text{FWHM } \beta_{\text{Sample}} (°) = \sqrt{\text{FWHM } \beta_{\text{Total}} (°) - \text{FWHM } \beta_{\text{Instrument}} (°)}$$

where $\text{FWHM } \beta_{\text{Instrument}} (°) = 0.05022$.

The parameters of the four diffraction peaks extracted from the XRD patterns and the related profile-fitting results are listed in Table 2, using UDM analysis through the following Equation [11,42,43]:

$$\beta_{\text{hkl}} \cos \theta = \frac{k\lambda}{D} + 4\varepsilon \sin \theta$$

where D is crystal size, k is the shape factor (often about 0.9), λ is the incident X-ray wavelength, β_{hkl} is the full width at half maximum (FWHM) in radians, ε is the strain, and θ is the Bragg's angle.

Table 2. Parameters of the (110), (220), (310), and (224) diffraction peaks extracted from the XRD patterns and the related profile-fitting results from the W-H plot.

Solvent	D (nm)	Micro Strain $\varepsilon \times 10^{-4}$	Dislocation Density $\delta \times 10^{-3}$ (nm)$^{-4}$
DMF	56.82	22.60	3.10
DMSO	42.65	9.21	5.50
GBL	25.52	6.46	15.35

Figure 2 (insets) shows the plot of $4 \sin \theta$ vs. $\beta_{\text{hkl}} \cos \theta$, which results in a straight line whose slope and intercept are ε and $\frac{k\lambda}{D}$, respectively.

From Table 2, the crystallites sizes (D) decrease with the increasing dipole moment or polarity of the solvents (Table 1), which corresponds with the increase of XRD peaks broadening (FWHM) for DMF, DMSO, and GBL solvents, respectively. The increases in the crystallite size meet with reductions in both dislocation density and lattice strain. Lattice strain, an abundance of interfaces, or a large density of dislocations are frequently used to explain conductivity aberrations from single crystal or polycrystalline behavior. So, the dislocation density in the film is used as an indicator of the quality of the film. Table 2

demonstrates the difference in grain formation in a thin layer, which is attributed to several effects, including surface energy anisotropy. Furthermore, there are usually no dislocations at the film/substrate interface, which produces strains in the film. This will result in an increase in grain growth rates in the film, which will alleviate strains [44,45]. The induced lattice strain influences the crystallinity of the sample [46]. The reduction in lattice strain shows that the presence of guest elements reduces the density of crystal defects. The XRD pattern of the film made using DMSO features peaks with a higher intensity than those in the patterns of the other samples, which may be attributed to this film being slightly thicker than the others or being more completely crystallized, compared to the other films made using GBL and DMF. Moreover, the DMSO films are majorly PbI_2 based on XRD data. The patterns of the films show that the materials are polycrystalline in nature. The crystallinity shown in the SEM images presented in Figure 3 is agreeably reflected in the optical quality of the films, which will be discussed later in Section 3.2.

Figure 3a–c presents the top-view SEM images of the $MAPbI_3$ perovskite films, from which it can be seen that unique crystalline features can be observed for the perovskite films, with particle size length scales on the order of several hundreds of nanometers [17].

(a)

(b)

(c)

(d)

Figure 3. *Cont.*

(**e**)   (**f**)
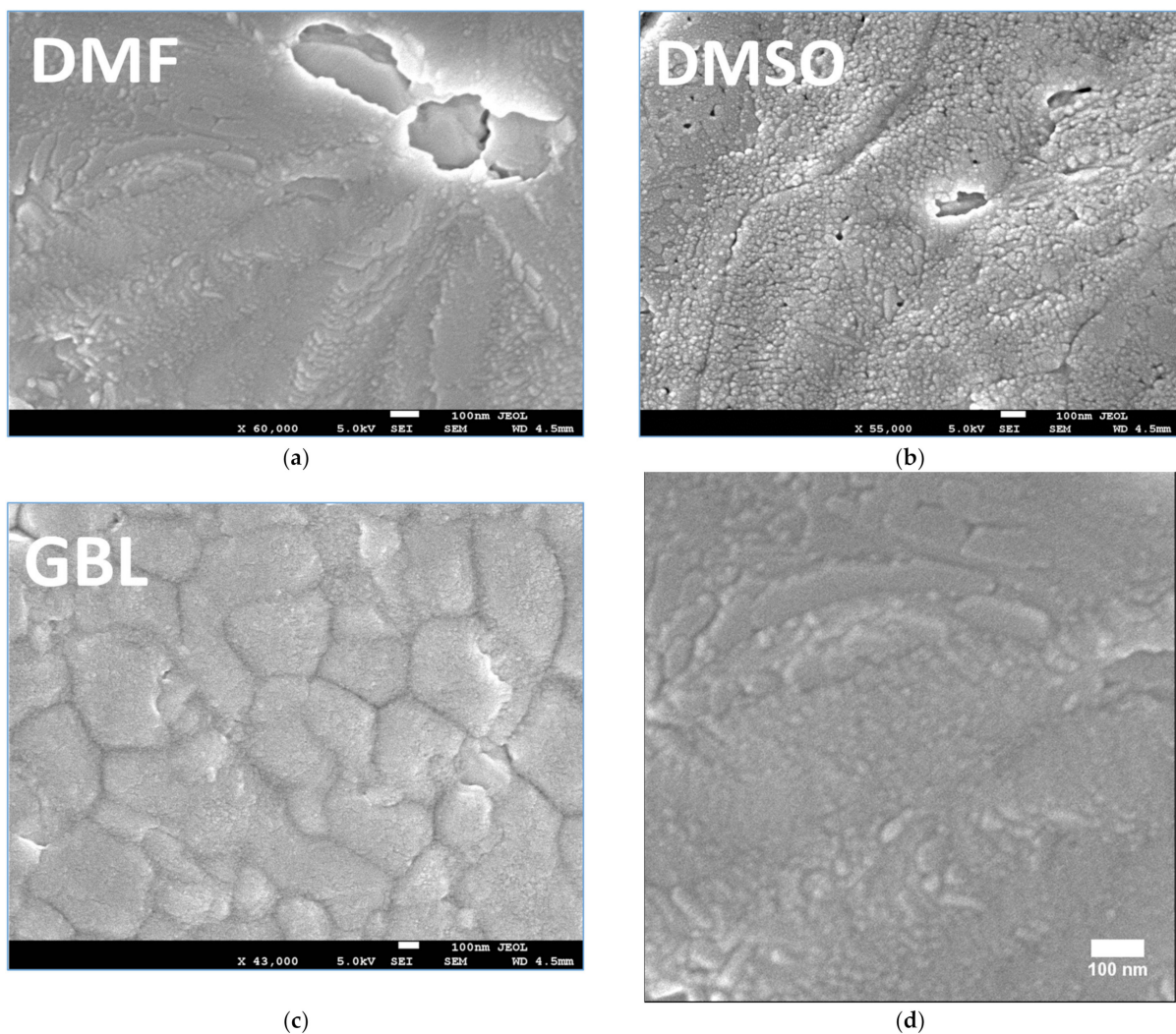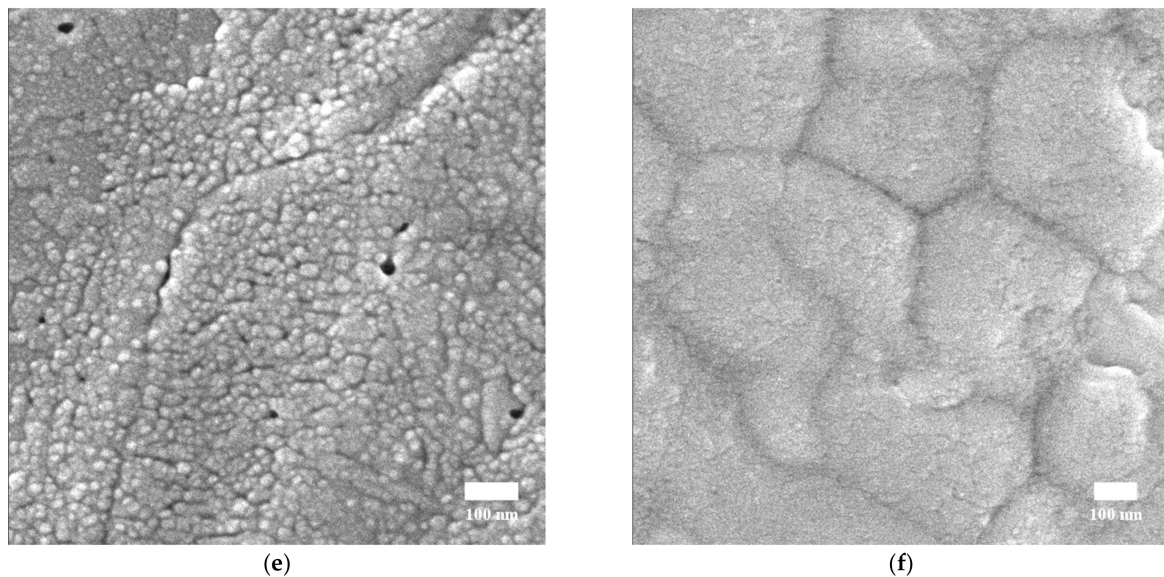
Figure 3. (**a**–**c**) Top-view SEM images of the MAPbI$_3$ perovskite films prepared using different solvents. Scale bars = 100 nm. (**d**–**f**) SEM images of the MAPbI$_3$ perovskite films.

The SEM image of the film prepared using DMF shown in Figure 3a shows almost complete coverage of the substrate with one big void. Although the film prepared using DMSO can be seen to have relatively smaller voids and nearly complete coverage of the substrate, it has uneven crystal domains and small-sized grains, as shown in Figure 3b. The film prepared using GBL shown in Figure 3c large voids can be observed between the crystal boundaries, indicating that this perovskite film does not completely cover the substrate. As can be seen by comparing the SEM images, the morphology of the film prepared using GBL (Figure 3c) is markedly different from the morphologies of the films prepared using DMF and DMSO (Figure 3a,b). The film prepared using GBL has large-sized crystals and that prepared using DMF shows anomalous crystals with a great number of pinholes, whereas that prepared using DMSO has a large number of needle-shaped perovskite crystals with pinholes, as can be seen in Figure 3d–f.

In Table 2, the crystal size of perovskite was estimated by using the FWHM value calculated for the (110) peak and applied using Scherrer's equation. SEM image processing by ImageJ free software was used to determine the range of particle sizes for DMF, DMSO, and GBL solvent, respectively (Figure 3d–f). The range of particle sizes are (46–90 nm), (17–45 nm), and (200–600 nm) for DMF, DMSO, and GBL, respectively. The crystallite sizes decrease with the increasing dipole moment of the solvents and the increase in growth of particle size, as well as the increased growth in crystallites in an identical growing environment [10,47]. Despite the high dipole moment of GBL solvent, the particles in this solvent are large-sized, as can be seen in Figure 3f. This finding is attributed to the solubility of MAPbI$_3$ precursors in GBL being lower than the DMF and DMSO solvents [48,49]. Meanwhile, the dielectric properties of the solvents play a significant role in the nucleation of the particles. Moreover, a high dielectric constant tends to stabilize the ions [47,50–53]. Based on these values, it is obvious that the perovskite crystals' sizes changed dramatically, affecting the shape of the X-ray diffraction patterns. The crystal sizes reported for DMF and DMSO samples using both approaches are consistent, confirming that Scherrer's equation is a useful tool for determining the crystal size for nanocrystals. This is not the case for micron crystals because the equation's constraints prevent determining their crystal size [54]. As a result, the broad peaks of the GBL patterns are not always associated with disordered crystalline formations.

3.2. Optical Properties

Figure 4 shows the UV-Vis-NIR absorbance spectra of the perovskite films, recorded by a spectrophotometer equipped with an absolute specular reflectance attachment. The films exhibit broad absorption, ranging from the visible to the NIR region for all solvents, whereas the GBL, DMF, and DMSO exhibit the most, moderate, and lowest absorption at the band edge, respectively. A surface profilometer (Bruker's Dektak 150, Bruker, Billerica, MA, USA) was used to measure the thin film thickness, which was 300, 350, and 327 nm for GBL, DMSO, and DMF thin films, respectively, with a thickness fluctuation of less than 10% over the entire film. Although the absorbance is affected by the layer thickness, the efficiency of the photon's absorption, as shown in Figure 4, can be considered as due to the inverse relationship between the efficiency with the film thickness here.
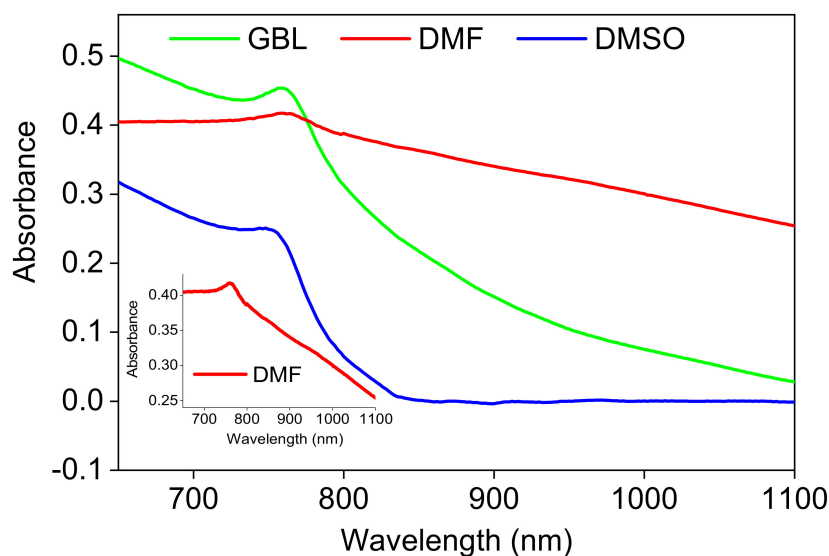
Figure 4. Absorbance spectra of the MAPbI$_3$ perovskite thin films made in various solvents.

In addition, the absorption spectrum shows clear different excitonic behavior at the band edge. According to the previous study [55], the band gap was estimated using the peak position of the absorption spectra to 1.623, 1.632, and 1.625 eV for DMF, DMSO, and GBL, respectively. However, it is better to conclude the band gap from the absorption coefficient, as shown in Figure 5, due to the absorption coefficient spectra being independent of the thickness of the film and maybe representative of the film quality [56].
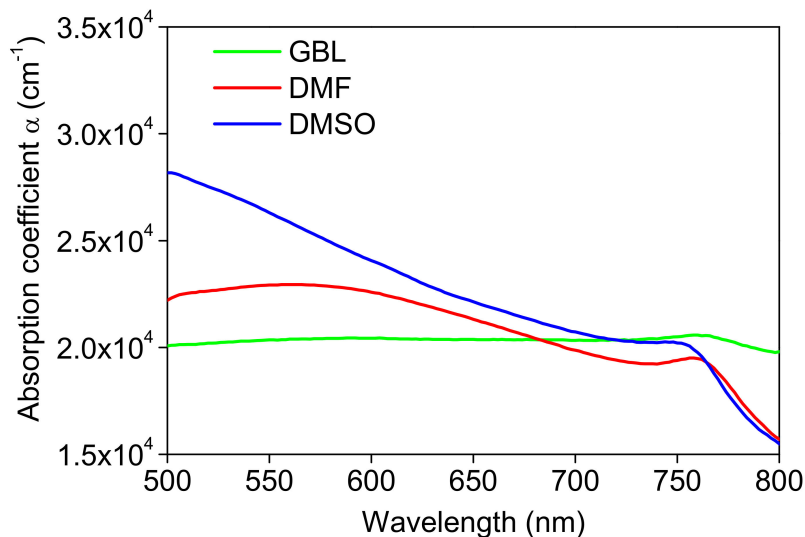
Figure 5. Absorption coefficient of the MAPbI$_3$ perovskite thin films prepared using different solvents.

The GBL film shows the highest optical density among the films despite being the thinnest film, due to it being majorly PbI_2 based on XRD data. The high absorption peak intensity in the solar spectrum region provides a substantial potential for fully utilizing the energy of photons with energies greater than the bandgap, providing information about light-harvesting capabilities and improving charge collection at the solar cell electrodes [11].

From the SEM, XRD, and UV-Vis-NIR absorption results, the slight differences in the measurements in both the XRD and UV-Vis-NIR results of the perovskite films made in various solvents indicate that the solvent effect only affects the coverage and shape of the film without creating significant changes in the optical characteristics of crystal structures of the films.

The absorption coefficient (α) as a measure of direct transition was determined (Figure 5) using the equation $\alpha = 2.303 \times A/d$, where (A) and (d) represent the absorbance and the film thickness, respectively. As mentioned above, the film's thicknesses were measured by a surface profilometer around 300, 350, and 327 nm for GBL, DMSO, and DMF thin films, respectively. So, the absorption coefficient values are summarized in Table 3. These values were taken at 532 nm, which will be used as the excitation wavelength to pump the sample and obtain the PL spectra, as will be discussed later.

Table 3. Optical constants of the $MAPbI_3$ thin films prepared using different solvents.

Optical Parameter	DMF	DMSO	GBL
λ_{ABS}(nm)	761	750	759
α (μm^{-1})	1.96	1.99	2.06
δ_p (μm)	0.51	0.50	0.94
E_g (eV)	1.623	1.632	1.625
PL Peak (nm)	787.7	787.9	782.5
ASE Peak (nm)	789.5	788.2	783.5
ASE FWHM (nm)	11.19	13.98	13.43

So, we conclude that the bandgap energy of the films prepared with different solvents increases with the increase of the solvent dipole moment, which corresponds with the decrease in crystallites and particle size. The GBL behavior is also discussed in the SEM discussion (Section 3.1). The huge variation in the band gap and light absorption properties of perovskites layer sensitively depend on the composition [57,58]. The different Urbach tail behavior and the variability in the E_g values of the films prepared in different solvents can be attributed to the differences in the microstructures and morphologies of the films, which lead to them having differences in inter-atomic bonding.

All samples were excited by 532 nm under high-energy excitation. Then, the PL emission spectra (Figure 6) were recorded and found to be centered at 787.6, 787.9, and 782.5 nm in relation to the absorption profiles of the films prepared using DMF, DMSO, and GBL, respectively. So, bandgap and PL positions are usually solvent dependent, attributed to decreases of the crystallite size of the particles with the increasing dipole moment or polarity of the solvents. The PL spectra are shifted with the change in solvent polarity due to solvent relaxation, so the absorption spectra are preferred for bandgap calculations. When the polarity index and dielectric constant of the solvents for DMF and DMSO are increased, the wavelength moves towards a longer wavelength (redshift) [47,59,60].

As mentioned in the experimental section, equimolar ratios of MAI and PbI_2 were mixed together to produce a 30 wt.% precursor solution of $MAPbI_3$ using GBL, DMF, and DMSO as the processing solvents to getting colloidal solutions with identical concentrations. Then, the three solutions were spin-coated on glass substrates with the same experimental conditions.
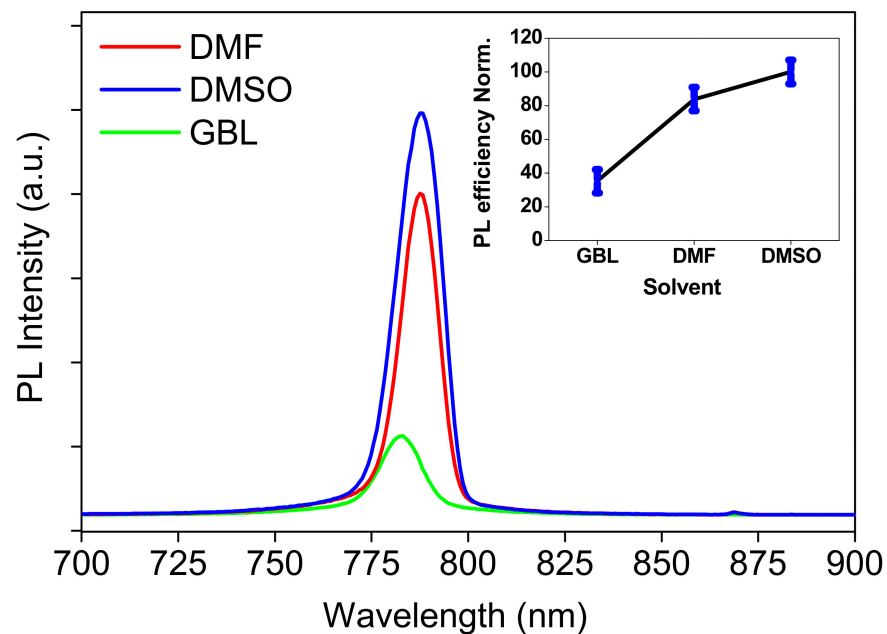
Figure 6. PL spectra of the MAPbI$_3$ perovskite thin films prepared using different solvents, for 532 nm as excitation wavelength for all samples. The insets show normalized PL efficiencies with statistical distribution (error bar) of the prepared films for three solvents.

Commonly, the higher PL intensity signifies the higher PLQY. However, this is true only if the thickness of the sample or concentration (if colloidal solution) is identical. Here, the observed change in the PL intensity is around 20% and 60% for DMF and GBL, respectively, compared to the DMSO as the higher one. In general, the change in the PL intensity of the results was larger than 10%, which was greater than the error in the film thickness variation over the entire film, in addition to the other experimental errors. Moreover, the observed change in the PL intensity is greater than the thickness variation itself, namely 7% and 14% for DMF and GBL, respectively, compared to the DMSO. So, this discussion enables us to compare the effect of solvent from the PL intensity. In addition, the higher PL intensity signifies the higher PLQY, which suggests that the sample has a high luminescence capacity, and the narrow line-width (FWHM) indicates that the pure colors are emitted [61]. The measurements of PL under high-energy excitation, as mentioned above, reflected the narrower line-width than the reported results.

The higher PL quantum yield for the film prepared in DMSO (as shown in Figure 6 (insets)) reflects its high content of the residue of PbI$_2$ on the surface of the perovskite thin film, as shown in Figure 3b. Specifically, the films prepared in DMF and DMSO have the best optical quality and crystallinity, as shown in Figures 2 and 3, whereas the GBL behavior is also mentioned in the SEM discussion (Section 3.1). This means that the PL intensity can be attributed to the nature of the chemical interaction between the perovskite precursors and solvent or correlated to the dielectric constant of solvent DMSO, which has a large dielectric value [47,59,60].

From the results listed above in both SEM images, XRD patterns, and PL spectroscopic investigations, we expect a significant decrease in the ability of the carriers to inject electrons into the perovskite layer prepared by DMSO solvent [36,41]. This can be attributed to the uneven crystal domains and small-sized grains, as well as the large number of needle-shaped perovskite crystals with pinholes, the high of the residue of PbI$_2$ on the perovskite film surface, and the higher electron-hole recombination, respectively, during the use of DMSO. As a result, it can be stated that the GBL is the best so far for preparing perovskite-based solar cells.

From all this, we conclude that for a thin photovoltaic film, optical characteristics management is critical for harvesting light, and its ability is limited by absorption band width and absorption coefficients in terms of ensuring high efficiency [62].

Finally, to assess the appropriateness of the MAPbI$_3$ perovskite-based thin films as a gain medium in comparison to the light amplification properties of them for three types of solvents, PL spectra as a function of the pumping energy density were studied. In general, the normal PL spectra are called spontaneous emission, whereas at the high energy excitation the PL is called stimulated emission or amplified spontaneous emission (ASE). The PL spectra of thin films prepared by three types of solvents under high energy excitation will be used as a benchmark for this reason. In addition, by examining the ASE properties, we may examine the thin film's viability as a gain medium when excited to induce a population inversion in the laser system. Experimentally, samples of the films were excited using a 532 nm, 11 ns pulsed laser, with a pump fluence of ~2 mJ/cm^2 to bring the samples to an ASE state.

Figure 7 shows the PL spectra of the MAPbI$_3$ perovskite thin films prepared using different solvents under high-energy excitation. By comparing spontaneous emission under low energy excitation or below threshold (Figure 6) and stimulated emission under high energy excitation or above threshold (Figure 7), the following can be notice: the PL spectrum was broad and featureless at low pump energy, but when the pump energy exceeded a crucial point known as the ASE threshold, three events occurred simultaneously, demonstrating the switch from spontaneous to stimulated emission (ASE state). Moreover, the simultaneous occurrence of the following three phenomena is characteristic of determining the specific energy density threshold of the transition from SE to ASE: spectral narrowing of the emission, the nonlinear increase of the emission density of the active material versus the pump energy density, and the appearance of an ASE peak near the long-wavelength region of spontaneous emission, which grows very fast with the pump energy beyond the threshold [2,37].
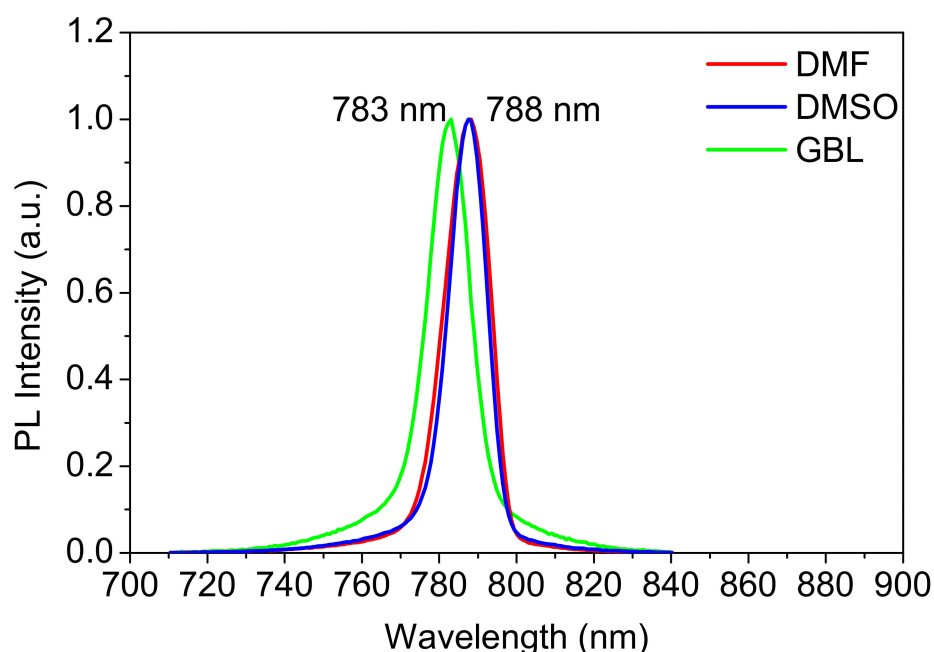
Figure 7. PL spectra of the MAPbI$_3$ perovskite thin films prepared using different solvents under high energy excitation.

Here, all samples were excited by 532 nm. Then, the PL emission spectra (Figure 7) were recorded and found to be centered at 788.2, 789.5, and 783.5 nm in relation to the absorption and normal PL profiles of the films prepared using DMSO, DMF, and GBL, respectively. The red-shifted high energy excitation was shown for all samples. The trend

is comparable, and the sensitivity of the ASE peak position to excitation pumping energy is generally consistent across all films. The line width at half maximum (FWHM) in the ASE state becomes narrower than in spontaneous emission. The FWHM are 13.98, 11.19, and 13.43 for DMSO, DMF, and GBL, respectively. Usually, the PL peak and FWHM are characteristic factors related to the constituents and disorder in thin films.

4. Conclusions

$MAPbI_3$ perovskite films were deposited on glass substrates via a single-step, low-temperature solution method. In this work, both the morphology and surface coverage of the films were controlled using DMF, DMSO, and GBL as the solvent to make a perovskite solution from the perovskite precursors. The XRD, SEM, and UV-Vis spectroscopy results show that the coverage of the $MAPbI_3$ perovskite films is not intrinsically homogeneous, particularly in terms of the great variation observed in crystallites and particle size and aggregation. These film characteristics were found to be solvent dependent during the deposition of the $MAPbI_3$ perovskite films on the substrates. Moreover, the results show how the optical quality of the films can be correlated to their crystalline quality according to the different solvents used. In addition, these results suggest that the synthesized films prepared using DMSO, DMF, and GBL exhibit the best crystallinity and optical characteristics (photoluminescence (PL)), respectively. Furthermore, a typical polar solvent for PbI_2 is another effect influencing the appearance of PbI_2 peaks in XRD data. The PbI_2 peak was stronger for DMSO rather than the others, GBL and DMF, due to DMF being a common polar solvent for perfectly dissolved PbI_2. The film prepared using GBL has large-sized crystals and that prepared using DMF shows anomalous crystals with a great number of pinholes, whereas that prepared using DMSO has a large number of needle-shaped perovskite crystals with pinholes.

The film prepared in DMSO shows the highest transmittance and the highest bandgap energy of the prepared films. The GBL film shows the highest optical density among the films, despite being the thinnest film, due to it being majorly PbI_2 based on XRD data.

Finally, using different solvents to process the solution of the perovskite precursor shows how the interfacial contacts can be improved through fabricating perovskite film by smoothing, further contributing to a uniform crystal domain with large-sized grains. These improvements contribute toward the optimization of perovskite film morphology for the use of these materials in high-performance photovoltaic applications.

References

1. Yin, W.-J.; Shi, T.; Yan, Y. Unique properties of halide perovskites as possible origins of the superior solar cell performance. *Adv. Mater.* **2014**, *26*, 4653–4658. [CrossRef] [PubMed]
2. Park, N.G. Organometal perovskite light absorbers toward a 20% efficiency low-cost solid-state mesoscopic solar cell. *J. Phys. Chem. Lett.* **2013**, *4*, 2423–2429. [CrossRef]
3. Qaid, S.M.H.; Al Sobaie, M.S.; Majeed Khan, M.A.; Bedja, I.M.; Alharbi, F.H.; Nazeeruddin, M.K.; Aldwayyan, A.S. Band-gap tuning of lead halide perovskite using a single step spin-coating deposition process. *Mater. Lett.* **2016**, *164*, 498–501. [CrossRef]
4. Alcocer, M.J.P.; Leijtens, T.; Herz, L.M.; Petrozza, A.; Snaith, H.J. Electron-hole diffusion lengths exceeding 1 micrometer in an organometal trihalide perovskite absorber. *Science* **2014**, *342*, 341–344.
5. Adjokatse, S.; Fang, H.H.; Loi, M.A. Broadly tunable metal halide perovskites for solid-state light-emission applications. *Mater. Today* **2017**, *20*, 413–424. [CrossRef]
6. Hirasawa, M.; Ishihara, T.; Goto, T.; Uchida, K.; Miura, N. Magnetoabsorption of the lowest exciton in perovskite-type compound $(CH_3NH_3)PbI_3$. *Phys. B* **1994**, *201*, 427–430. [CrossRef]
7. Tanaka, K.; Takahashi, T.; Ban, T.; Kondo, T.; Uchida, K.; Miura, N. Comparative study on the excitons in lead-halide-based perovskite-type crystals $CH_3NH_3PbBr_3$ $CH_3NH_3PbI_3$. *Solid State Commun.* **2003**, *127*, 619–623. [CrossRef]
8. Ishihara, T. Optical properties of PbI-based perovskite structures. *J. Lumin.* **1994**, *60–61*, 269–274. [CrossRef]
9. Shen, Q.; Ogomi, Y.; Chang, J.; Tsukamoto, S.; Kukihara, K.; Oshima, T.; Osada, N.; Yoshino, K.; Katayama, K.; Toyoda, T.; et al. Charge transfer and recombination at the metal oxide/$CH_3NH_3PbClI_2$/spiro-OMeTAD interfaces: Uncovering the detailed mechanism behind high efficiency solar cells. *Phys. Chem. Chem. Phys.* **2014**, *16*, 19984. [CrossRef]
10. Pang, S.; Chen, D. High-Quality Perovskite Film Preparations for Efficient Perovskite Solar Cells. In *Emerging Solar Energy Materials*; InTech: Houston, TX, USA, 2018; p. 217.
11. Al-Asbahi, B.A.; Qaid, S.M.H.; Hezam, M.; Bedja, I.; Ghaithan, H.M.; Aldwayyan, A.S. Effect of deposition method on the structural and optical properties of $CH_3NH_3PbI_3$ perovskite thin films. *Opt. Mater.* **2020**, *103*, 109836. [CrossRef]
12. Eperon, G.E.; Burlakov, V.M.; Docampo, P.; Goriely, A.; Snaith, H.J. Morphological control for high performance, solution-processed planar heterojunction perovskite solar cells. *Adv. Funct. Mater.* **2014**, *24*, 151–157. [CrossRef]
13. Mhamdi, A.; Mehdi, H.; Bouazizi, A. Effect of solvents and annealing treatment on the properties of the methylammonium lead tribromide perovskite thin films. *J. Mater. Sci. Mater. Electron.* **2021**, *32*, 2302–2311. [CrossRef]
14. Mutlu, A.; Yeşil, T.; Zafer, C. Utilization of coordinating green solvents for high quality methylammonium bismuth iodide thin films for photovoltaic applications. *Org. Electron.* **2021**, *95*, 106191. [CrossRef]
15. You, J.; Hong, Z.; Song, T.B.; Meng, L.; Liu, Y.; Jiang, C.; Zhou, H.; Chang, W.H.; Li, G.; Yang, Y. Moisture assisted perovskite film growth for high performance solar cells. *Appl. Phys. Lett.* **2014**, *105*, 183902. [CrossRef]
16. Dualeh, A.; Tétreault, N.; Moehl, T.; Gao, P.; Nazeeruddin, M.K.; Grätzel, M. Effect of annealing temperature on film morphology of organic-inorganic hybrid pervoskite solid-state solar cells. *Adv. Funct. Mater.* **2014**, *24*, 3250–3258. [CrossRef]
17. Burschka, J.; Pellet, N.; Moon, S.-J.; Humphry-Baker, R.; Gao, P.; Nazeeruddin, M.K.; Grätzel, M. Sequential deposition as a route to high-performance perovskite-sensitized solar cells. *Nature* **2013**, *499*, 316–319. [CrossRef]
18. Jung, H.S.; Park, N.G. Perovskite solar cells: From materials to devices. *Small* **2015**, *11*, 10–25. [CrossRef]
19. Liu, M.; Johnston, M.B.; Snaith, H.J. Efficient planar heterojunction perovskite solar cells by vapour deposition. *Nature* **2013**, *501*, 395–398. [CrossRef]
20. Kim, B.-S.; Choi, M.-H.; Choi, M.-S.; Kim, J.-J. Composition-controlled organometal halide perovskite via CH_3NH_3I pressure in a vacuum co-deposition process. *J. Mater. Chem. A* **2016**, *4*, 5663–5668. [CrossRef]
21. Song, T.; Chen, Q.; Zhou, H.; Jiang, C.; Wang, H.; Yang, M.; Liu, Y. Perovskite solar cells: Film formation and properties. *J. Mater. Chem. A* **2015**, *3*, 9032–9050. [CrossRef]
22. Zhao, Y.; Zhu, K. CH_3NH_3Cl-assisted one-step solution growth of $CH_3NH_3PbI_3$: Structure, charge-carrier dynamics, and photovoltaic properties of perovskite solar cells. *J. Phys. Chem. C* **2014**, *118*, 9412–9418. [CrossRef]
23. Im, J.H.; Kim, H.S.; Park, N.G. Morphology-photovoltaic property correlation in perovskite solar cells: One-step versus two-step deposition of $CH_3NH_3PbI_3$. *APL Mater.* **2014**, *2*, 081510. [CrossRef]
24. Lv, S.; Pang, S.; Zhou, Y.; Padture, N.P.; Hu, H.; Wang, L.; Zhou, X.; Zhu, H.; Zhang, L.; Huang, C.; et al. One-step, solution-processed formamidinium lead trihalide ($FAPbI_{(3-x)}Cl_x$) for mesoscopic perovskite–polymer solar cells. *Phys. Chem. Chem. Phys.* **2014**, *16*, 19206–19211. [CrossRef] [PubMed]
25. Kim, H.-B.; Choi, H.; Jeong, J.; Kim, S.; Walker, B.; Song, S.; Kim, J.Y. Mixed solvents for the optimization of morphology in solution-processed, inverted-type perovskite/fullerene hybrid solar cells. *Nanoscale* **2014**, *6*, 6679. [CrossRef]
26. Liu, R.; Xu, K. Solvent engineering for perovskite solar cells: A review. *Micro Nano Lett.* **2020**, *15*, 349–353. [CrossRef]
27. Rong, Y.; Tang, Z.; Zhao, Y.; Zhong, X.; Venkatesan, S.; Graham, H.; Patton, M.; Jing, Y.; Guloy, A.M.; Yao, Y. Solvent engineering towards controlled grain growth in perovskite planar heterojunction solar cells. *Nanoscale* **2015**, *7*, 10595–10599. [CrossRef]
28. Cai, B.; Zhang, W.H.; Qiu, J. Solvent engineering of spin-coating solutions for planar-structured high-efficiency perovskite solar cells. *Cuihua Xuebao Chin. J. Catal.* **2015**, *36*, 1183–1190. [CrossRef]
29. Hwang, K.H.; Nam, S.H.; Kim, D.I.; Seo, H.J.; Boo, J.H. The influence of DMSO and ether via fast-dipping treatment for a perovskite solar cell. *Sol. Energy Mater. Sol. Cells* **2018**, *180*, 386–395. [CrossRef]

30. Fang, X.; Wu, Y.; Lu, Y.; Sun, Y.; Zhang, S.; Zhang, J.; Zhang, W.; Yuan, N.; Ding, J. Annealing-free perovskite films based on solvent engineering for efficient solar cells. *J. Mater. Chem. C* **2017**, *5*, 842–847. [CrossRef]

31. Liu, X.; Wu, J.; Yang, Y.; Wu, T.; Guo, Q. Pyridine solvent engineering for high quality anion-cation-mixed hybrid and high performance of perovskite solar cells. *J. Power Sources* **2018**, *399*, 144–150. [CrossRef]

32. Wu, T.; Wu, J.; Tu, Y.; He, X.; Lan, Z.; Huang, M.; Lin, J. Solvent engineering for high-quality perovskite solar cell with an efficiency approaching 20%. *J. Power Sources* **2017**, *365*, 1–6. [CrossRef]

33. Seo, J.; Park, S.; Chan Kim, Y.; Jeon, N.J.; Noh, J.H.; Yoon, S.C.; Seok, S. Il Benefits of very thin PCBM and LiF layers for solution-processed p–i–n perovskite solar cells. *Energy Environ. Sci.* **2014**, *7*, 2642–2646. [CrossRef]

34. Jeon, N.J.; Noh, J.H.; Kim, Y.C.; Yang, W.S.; Ryu, S.; Seok, S. Il Solvent engineering for high-performance inorganic–organic hybrid perovskite solar cells. *Nat. Mater.* **2014**, *13*, 897–903. [CrossRef] [PubMed]

35. Petrov, A.A.; Ordinartsev, A.A.; Fateev, S.A.; Goodilin, E.A.; Tarasov, A.B. Solubility of hybrid halide perovskites in dmf and dmso. *Molecules* **2021**, *26*, 7541. [CrossRef]

36. Saianand, G.; Sonar, P.; Wilson, G.J.; Gopalan, A.I.; Roy, V.A.L.; Unni, G.E.; Mamun Reza, K.; Bahrami, B.; Venkatramanan, K.; Qiao, Q. Current advancements on charge selective contact interfacial layers and electrodes in flexible hybrid perovskite photovoltaics. *J. Energy Chem.* **2021**, *54*, 151–173. [CrossRef]

37. Qaid, S.M.H.; Khan, M.N.; Alqasem, A.; Hezam, M.; Aldwayyan, A. Restraining effect of film thickness on the behaviour of amplified spontaneous emission from methylammonium lead iodide perovskite. *IET Optoelectron.* **2018**, *13*, 2–6. [CrossRef]

38. Zuo, C.; Ding, L. Drop-casting to make efficient perovskite solar cells under high humidity. *Angew. Chem.* **2021**, *133*, 11342–11346. [CrossRef]

39. Malinkiewicz, O.; Yella, A.; Lee, Y.H.; Espallargas, G.M.M.; Graetzel, M.; Nazeeruddin, M.K.; Bolink, H.J. Perovskite solar cells employing organic charge-transport layers. *Nat. Photonics* **2014**, *8*, 128–132. [CrossRef]

40. Etgar, L.; Gao, P.; Xue, Z.; Peng, Q.; Chandiran, A.K.; Liu, B.; Nazeeruddin, M.K.; Grätzel, M. Mesoscopic $CH_3NH_3PbI_3/TiO_2$ heterojunction solar cells. *J. Am. Chem. Soc.* **2012**, *134*, 17396–17399. [CrossRef]

41. Yao, Y.; Zou, X.; Cheng, J.; Ling, T.; Chang, C.; Chen, D. Influence of solution deposition process on modulating majority charge carrier type and quality of perovskite thin films for solar cells. *Materials* **2019**, *12*, 2494.

42. Nath, D.; Singh, F.; Das, R. X-ray diffraction analysis by Williamson-Hall, Halder-Wagner and size-strain plot methods of CdSe nanoparticles- a comparative study. *Mater. Chem. Phys.* **2020**, *239*, 122021. [CrossRef]

43. Qaid, S.M.; Ghaithan, H.M.; Al-Asbahi, B.A.; Aldwayyan, A.S. Tuning of amplified spontaneous emission wavelength for green and blue light emission through the tunable composition of $CsPb(Br_{1-x}Cl_x)_3$ inorganic perovskite quantum dots. *J. Phys. Chem. C* **2021**, *125*, 9441–9452. [CrossRef]

44. Thompson, C.V.; Carel, R. Stress and grain growth in thin films. *J. Mech. Phys. Solids* **1996**, *44*, 657–673. [CrossRef]

45. Qaid, S.M.H.; Al-Asbahi, B.A.; Ghaithan, H.M.; Aldwayyan, A.S. Tuning the optical properties of meh–ppv/pfo hybrid thin films via the incorporation of cspbbr3 quantum dots. *Coatings* **2021**, *11*, 154. [CrossRef]

46. Adhikari, G.C.; Thapa, S.; Yue, Y.; Zhu, H.; Zhu, P. Near unity plqy and high stability of barium thiocyanate based all-inorganic perovskites and their applications in white light-emitting diodes. *Photonics* **2021**, *8*, 209. [CrossRef]

47. Maharaz, M.N.; Halimah, M.K.; Paiman, S.; Saiden, N.M.; Alibe, I.M. Influence of solvents and irradiation time on structural and optical properties of cubic PbS nanoparticles. *Int. J. Electrochem. Sci.* **2018**, *13*, 9317–9332. [CrossRef]

48. Liu, Y.; Yang, Z.; Liu, S.F. Recent progress in single-crystalline perovskite research including crystal preparation, property evaluation, and applications. *Adv. Sci.* **2018**, *5*, 1700471. [CrossRef]

49. Saidaminov, M.I.; Abdelhady, A.L.; Maculan, G.; Bakr, O.M. Retrograde solubility of formamidinium and methylammonium lead halide perovskites enabling rapid single crystal growth. *Chem. Commun.* **2015**, *51*, 17658–17661. [CrossRef]

50. Cao, Y.; Hu, P.; Jia, D. Solvothermal synthesis, growth mechanism, and photoluminescence property of sub-micrometer PbS anisotropic structures. *Nanoscale Res. Lett.* **2012**, *7*, 668. [CrossRef]

51. Alagumuthu, G.; Kirubha, R. Synthesis and characterisation of silver nanoparticles in different medium. *Open J. Synth. Theory Appl.* **2012**, *1*, 13–17. [CrossRef]

52. Sathyamoorthy, R.; Kungumadevi, L. Facile synthesis of PbS nanorods induced by concentration difference. *Adv. Powder Technol.* **2015**, *26*, 355–361. [CrossRef]

53. Kumar, S.A.; Saravanan, V.; Rajasimman, M. Microwave mediated synthesis and characterizations of CdO nanoparticles. *J. Adv. Chem. Sci.* **2015**, *1*, 133–138.

54. Londoño-Restrepo, S.M.; Jeronimo-Cruz, R.; Millán-Malo, B.M.; Rivera-Muñoz, E.M.; Rodriguez-García, M.E. Effect of the nano crystal size on the X-ray diffraction patterns of biogenic hydroxyapatite from human, bovine, and porcine bones. *Sci. Rep.* **2019**, *9*, 5915. [CrossRef] [PubMed]

55. Adhikari, G.C.; Vargas, P.A.; Zhu, H.; Grigoriev, A.; Zhu, P. Tetradic phosphor white light with variable CCT and superlative CRI through organolead halide perovskite nanocrystals. *Nanoscale Adv.* **2019**, *1*, 1791–1798. [CrossRef]

56. Zhang, L.; Zuo, C.; Ding, L. Efficient $MAPbI_3$ solar cells made via drop-coating at room temperature. *J. Semicond.* **2021**, *42*, 072201. [CrossRef]

57. Yanagida, M.; Shirai, Y.; Khadka, D.B.; Miyano, K. Photoinduced ion-redistribution in $CH_3NH_3PbI_3$ perovskite solar cells. *Phys. Chem. Chem. Phys.* **2020**, *22*, 25118–25125. [CrossRef]

58. Ghaithan, M.H.; Qaid, S.M.H.; Alahmed, Z.A.; Hezam, M.; Lyras, A.; Amer, M.; Aldwayyan, A.S. Anion substitution effects on the structural, electronic, and optical properties of inorganic $CsPb(I_{1-x}Br_x)_3$ and $CsPb(Br_{1-x}Cl_x)_3$ perovskites: Theoretical and experimental approaches. *J. Phys. Chem. C* **2021**, *125*, 886–897. [CrossRef]

59. Al Mohaimeed, R.M.; Ansari, A.A.; Aldwayyan, A. The role of solvent environment on the optical behavior of chemically synthesized silicon nanoparticles. *J. Spectrosc.* **2018**, *2018*, 6870645. [CrossRef]

60. Khan, M.N.; Khan, M.A.M.; Al Dwayyan, A.S.; Labis, J.P.; Yu, W.W. Comparative study on electronic, emission, spontaneous property of porous silicon in different solvents. *J. Nanomater.* **2014**, *2014*, 682571. [CrossRef]

61. Adhikari, G.C.; Thapa, S.; Zhu, H.; Zhu, P. UV resin enhanced stability of metal halide perovskite nanocrystals for white light-emitting diodes. *ACS Appl. Electron. Mater.* **2020**, *2*, 35–40. [CrossRef]

62. Kojima, A.; Teshima, K.; Shirai, Y.; Miyasaka, T. Organometal halide perovskites as visible-light sensitizers for photovoltaic cells. *J. Am. Chem. Soc.* **2009**, *131*, 6050–6051. [CrossRef] [PubMed]